β-actin plasticity is modulated by coordinated actions of histidine 73 methylation, nucleotide type, and ions

Adrien Schahl[1,2], **Louis Lagardere**[2], **Brandon Walker**[3], **Pengyu Ren**[3], **Antoine Jégou**[4], **Matthieu Chavent**[1*], **Jean-Philip Piquemal**[2*]

***For correspondence:** matthieu.chavent@ipbs.fr, jean-philip.piquemal@sorbonne-universite.fr ( )

[1]Institut de Pharmacologie et de Biologie Structurale, Université de Toulouse, CNRS, Université Paul Sabatier, 31400 Toulouse, France; [2]Sorbonne Université, LCT, UMR 7616 CNRS, F-75005, Paris, France; [3]Department of Biomedical Engineering, The University of Texas at Austin, Austin, Texas 78712, United States; [4]Université Paris Cité, CNRS, Institut Jacques Monod, F-75013 Paris, France

Abstract Actin undergoes important structural changes to transition from the G-actin to the F-actin form. Furthermore, mammals express different isoforms, with only slight variations at the amino acid level. While the α-skeletal actin isoform was thoroughly studied using molecular dynamics simulations, the dynamics of the β-actin isoform remains unexplored. Here, we have used the AMOEBA polarizable force field coupled with adaptive sampling to investigate the plasticity of the β-actin. This highlighted the role of a post translational modification, i.e. the histidine 73 methylation, to enhance the opening of the actin cleft and change allosteric paths linking the two distant subdomains SD2 and SD4. The action of the methylation can be also modulated by the type of nucleotide bound in the actin cavity and the type of ions surrounding the protein. Taken together, these results shed new lights onto the plasticity of the β-actin isoform and the coordinated role of several environmental factors. These results may help designing new types of molecules, such as allosteric modulators, specifically targeting the β-actin isoform.

Introduction

Actin is involved in numerous cellular functions, such as cell shape, proliferation, and migration (***Svitkina, 2018***). Different isoforms are expressed in function of the cell type (***Perrin and Ervasti, 2010***). Among them α-actin, one of the most studied isoforms, is only present in muscles while β-actin is ubiquitously expressed in the cytoplasm of cells and exhibits specific functions.

These isoforms share a common structure constituted by four subdomains undergoing conformational changes with large consequences at the molecular up to the supramolecular level (***Merino et al., 2020***). Above a critical concentration, several monomers assemble to form a filament (***Wegner, 1982***). In this configuration, the globular actin monomer (G-actin) adopts a flattened structure (F-actin), characterized by a lower dihedral angle constituted by the four subdomains (***Oda et al., 2009***). The actin structural plasticity is also important at the molecular level as, in the F-actin form, its ATPase activity is increased by four orders of magnitude in comparison of its G-actin form (***Blanchoin and Pollard, 2002***).

Table 1. Parameters of studied systems : isoform, post-translational modification of histidine 73 (HIS: unmodified and HIC: methylated), nucleotide type, ion types, Number of proteins, and initial structure.

Sequence	P.T.M.	Nucleotide	Ion (mM)	Number	Structure
α	HIS	ATP	150 KCl	Monomer	G
α	HIC	ATP	150 KCl	Monomer	G
β	HIS	ATP	150 KCl	Monomer	G
β	HIC	ATP	150 KCl	Monomer	G
β	HIC	ATP	75 $MgCl_2$	Monomer	G
β	HIS	ADP	150 KCl	Monomer	G
β	HIC	ADP	150 KCl	Monomer	G
β	HIC	ADP	75 $MgCl_2$	Monomer	G
β_{K118N}	HIC	ATP	150 KCl	Monomer	G
β_{K118N}	HIC	ADP	150 KCl	Monomer	G
β	HIC	ATP	150 KCl	4-mer	F
β	HIC	ADP	150 KCl	4-mer	F

Actin structural and dynamical properties can be modulated by an ensemble of environmental parameters (***Merino et al., 2020***; ***Varland et al., 2019***). Especially, the nucleotide state (ATP or ADP) changes the internal motions of the G-actin (***Ali et al., 2022***), and the stability (***Reynolds et al., 2022***) and formation rate (***Cooke, 1975***) of the filament. Furthermore, this rate is also greatly influenced by the type and concentration of ions (***Nyman et al., 2002***; ***Kang et al., 2012***). Beyond these two main parameters, recent work has also highlighted the importance of the methylation of histidine 73, a post-translational modification affecting filament formation (***Wilkinson et al., 2019***). This residue is located on the *sensor loop*. This loop undergoes structural rearrangements depending on the nucleotide state (***Graceffa and Dominguez, 2003***). Thus, histidine 73 methylation, ions concentration, and nucleotide states modulate the actin molecular and supramolecular properties but how they coordinate remains elusive.

Molecular Dynamics (MD) simulations have become increasingly popular over the last 20 years for studying biological systems at different scales (***Vanommeslaeghe et al., 2010***; ***Maier et al., 2015***; ***Souza et al., 2021***; ***Kim and Hummer, 2008***; ***Chu and Voth, 2005***). This method was extensively used to characterize properties of actin protein such as differences between nucleotide states (***Splettstoesser et al., 2009***; ***Saunders et al., 2014***; ***Jepsen and Sept, 2020***), waters located in the cavity and their impact on protein plasticity and enzymatic properties (***Saunders and Voth, 2011***; ***McCullagh et al., 2014***), interactions with small molecules (***Rennebaum and Caflisch, 2012***; ***Helal et al., 2013***) and the dynamics of filaments in various environments (***Chu and Voth, 2005***; ***Splettstoesser et al., 2011***; ***Zsolnay et al., 2020***; ***Schroer et al., 2020***; ***Shamloo and Mehrafrooz, 2018***; ***Jaswandkar et al., 2021***; ***Horan et al., 2020***; ***Castaneda et al., 2019***) but, to our knowledge, these computational works focus exclusively on α-actin while the β-actin isoform remains understudied.

Even if MD simulations have been instrumental in the understanding of how ion and water molecules interact with proteins (***Song et al., 2013***; ***Kopec et al., 2018***; ***Bellissent-Funel et al., 2016***), there is still room for improvement. While actin is known to be very plastic and the impact of ions and water molecules have been highlighted (***Hocky et al., 2016***; ***Kang et al., 2012***, ***2013***), the precise parametrization of these components is still challenging and depends on the system studied (***Kadaoluwa Pathirannahalage et al., 2021***). Recent methodological developments on polarizable force-fields have drastically increased the accuracy of interactions between these molecules and proteins (***Shi et al., 2015***; ***Melcr and Piquemal, 2019***; ***Jing et al., 2019***, ***2021***; ***Lynch et al., 2021***; ***El Ahdab et al., 2021***; ***Célerse et al., 2019***; ***Kratochvil et al., 2016***; ***Li et al., 2015***; ***El Khoury et al., 2022***). In addition, the use of enhanced sampling methods allows exploring diverse unknown states hard to reach through the use of classical molecular dynamics simulations (***Jaffrelot Inizan et al.,***

2021; *Bowman et al., 2010*; *Miao et al., 2015*; *Célerse et al., 2022*).

Here, we have deciphered the plasticity of β-actin by performing series of adaptive sampling simulations combined with the AMOEBA polarizable force field (Table 1). This allows us to assess the joint effects of histidine 73 methylation with ion concentration and nucleotide state on the plasticity of the isolated G-actin protein. We have also assessed how nucleotide state affects F-actin monomer at the barbed end of the filament. This work sheds new light onto the specific plasticity of the β-actin isoform and how it is finely modulated by several environmental factors. This may help the development of new strategies which precisely act on this isoform.

Results

Role of histidine 73 methylation on the global plasticity of ATP bound G-actin.

We performed 1.52 µs long adaptive sampling polarizable molecular dynamics simulations on both α- and β-actin isoforms containing ATP bound nucleotide and magnesium ion in the catalytic cavity (+150 mM of KCl). To assess the effect of the methylation of histidine 73 on the G-actin dynamics, we simulated both non-methylated histidine (HIS73) and methylated histidine (HIC73) and measured the dihedral angle formed by the four subdomains as well as the distance between SD2 and SD4, called cleft (Fig 1-A). For the β-actin without methylation, the protein fluctuated around a cleft of 25 Å and a dihedral angle of c.a. -20° (Fig 1-B). The histidine methylation clearly broadened the main basin affecting particularly the cleft distance, allowing a range of cleft distances from 25Å to 27Å, while the dihedral angle was slightly expanded. Thus, the methylation of histidine 73 led to a global change in the protein dynamics. This is also visible in the RMSF (Fig 1-C) where two areas, away from histidine 73, are affected by the methylation: the D-loop (Fig 1-A), and the SD4 subdomain. More precisely, the dynamics of helices around residues [200-206] and [228-232], situated at the opposite sides of SD4, were particularly affected by the methylation (Fig 1, D). Interestingly, even if the sequence identity between α and β-actin is very high (ca 94%), the histidine methylation seemed to affect the α isoform more (Fig S1) than the β isoform. The most affected areas for α-actin were comparable (Fig S2) with the ones seen on β-actin. Furthermore, both minima for dihedral angle and cleft were shifted in comparison to the β-actin isoform with respectively -17° and 27Å. Thus, the β-actin seems to display more subtle changes than the α-actin isoform. This may be related to their respective function in different tissues. For the following sections, we will focus on the β-actin isoform as little is known on the dynamics of this protein.

Histidine 73 methylation, SD2-SD4 bridge, and enzymatic cavity.

The [200-206] helix, situated in the SD4 subdomain, is close to the SD2 subdomain (Fig 1-C,D). For the non-methylated actin form, residues in this helix interacted with residues on the SD2 domain to bridge the two subdomains (Fig 2-A, left panel). Especially, GLU 207 formed stable hydrogen bonds with residue ARG 62 on SD2. With the methylation of histidine 73, these hydrogen bonds were clearly less stable (Fig 2-A, central panel), allowing the opening of the cleft (Fig 1-B, central panel). This opening was correlated with an increase of the volume cavity (Fig 2-B,C) passing from 680 $Å^3$ to 925 $Å^3$. Interestingly, for the methylated histidine, a second volume population started to appear around 870 $Å^3$. As this volume change may affect molecules inside the binding site, we checked the dynamical properties of the magnesium ion and water molecules around it. Even if the magnesium ion is still largely bound to the γ-phosphate of the ATP, in the methylated system, a higher unbound population can be observed (with a Mg^{2+}-γ-phosphate distance of around 4 Å), suggesting a more dynamical positioning of the magnesium ion (Fig 2-D). This is also correlated with a wider distribution of water molecules around the magnesium (Fig 2-E). So, histidine 73 may affect actin organization from the ATP binding site up to subdomain interactions.

Evolution of residues pathways bridging SD2 and SD4 subdomains.

Histidine 73 is near the geometrical center of the actin (Fig 1-A). Therefore its impact on SD2 and SD4 dynamics, especially on residues located at their extremities, doesn't appear obvious at first sight. This may imply an allosteric pathway to link these residues with the histidine. We therefore performed correlation-based dynamical network analysis (***Westerlund et al., 2020***; ***Melo et al., 2020***) to analyze the shortest paths between GLU207 and ARG62, residues involved in the most stable hydrogen bonds between SD2 and SD4. For actin containing the non methylated histidine, the 2 most representative shortest paths directly linked GLU207 and ARG62 (Fig 3-A, left and central panels). These two paths were overrepresented in comparison to the other paths (Table S1). The third most represented shortest path passed by residues PRO70 and GLU72, located on the sensor loop (Fig 3-A, right panel), displaying different conformations depending on the bound nucleotide (***Graceffa and Dominguez, 2003***). In this path, the formation of the [GLU72-ARG183] salt bridge linked the SD2 and SD4 subdomains. Interestingly, for the methylated histidine, residues involved in this latter path are all present in the most representative shortest path (Fig 3-B, left panel). In this path, there is no direct interaction between the extremities of SD2 and SD4 subdomains, meaning that the allosteric connection is achieved through the sensor loop. For the two most representative shortest paths the methylated histidine 73 was involved, while the third one displayed a SD2-SD4 bridge through interactions between TYR69 and ARG183. Interestingly, in the case of the methylated histidine 73, the paths propensities are clearly rebalanced with close probabilities for all the paths (Table S1). Taken together, these results suggest that histidine 73 methylation helps opening the cleft between SD2 and SD4 subdomain, otherwise mainly closed via the GLU207-ARG61 interactions. This methylation also affects allosteric paths joining SD2 and SD4 extremities rebalancing different paths and rerouting allosteric communications between the two subdomains via the sensor loop.

Modulation of histidine 73 methylation activity by ions.

Magnesium ion concentration plays an important role in actin polymerization (***Kang et al., 2012***). To analyse the effect of magnesium ions, we have replaced the 150 mM of KCl with 75 mM of $MgCl_2$. With the addition of magnesium ions, both cleft and dihedral angles were affected with respectively an increase in cleft opening (up to 30 Å) and dihedral angle (up to -30°) (Fig 1-B, right panel). The distribution of Mg^{2+} ions around the protein showed numerous areas of ions interactions spread on all the four subdomains (Fig S3). The residues were almost all negatively charged. Interestingly, GLU 72 on the sensor loop, was among the interacting residues. The RMSF (Fig 1-C) as well as the volume of the ATP binding cavity were affected by the addition of magnesium ions. The latter displayed a larger volume than without ions (Fig 1-C). The distribution of water molecules in the cavity is however quite narrow (Fig 1-E) with a Mg^{2+} ion in the cavity as stable as seen for the histidine 73 not methylated (Fig 1-D). The addition of magnesium ions also changed the allosteric paths between GLU207 and ARG62. As seen previously, the probability of apparition of the three most representative paths are relatively similar (Table S1). Interestingly, the most frequent path is no longer passing through the sensor loop but on the opposite side of the binding cavity (Fig 3-C, left panel). Hence, the addition of magnesium ions has a contrasted effect on the actin plasticity. On one hand, it favors the opening of the cleft and increases the dihedral angle. On the other hand, it limits the destabilizing effect of the histidine methylation at the binding site.

Limitation of actin plasticity by ADP nucleotide.

The type of nucleotide inside the enzymatic cavity seems to affect actin internal dynamics (***Ali et al., 2022***). Therefore, we have performed additional simulations with ADP in the binding cavity to compare with ATP bound actin. In presence of ADP, the enhanced internal flexibility of the actin monomer observed in the SD4 subdomain, for methylated histidine 73, was partially cancelled as

shown by a reduced RMSF (Fig 4-A). Both methylation of histidine 73 and addition of magnesium ions have little to no effect on the distribution of the dihedral angle and the cleft distance (Fig 4-B). This can be explained by sustained interactions between residues at the SD2-SD4 interface even with histidine methylation and magnesium ions (Fig 4-C). In this *closed* conformation, the volume of the binding cavity fluctuated less than in the ATP systems (Fig 4-D). Some differences can be noted regarding the positioning of the nucleotide and its bound magnesium (Fig4-E). In the case of methylated histidine, the magnesium ion inside the cavity was not directly bound to the β-phosphate of the ADP. It could be related to the higher number of water molecules structured around the ion (Fig 4-F). Similarly to ATP-bound systems, the addition of magnesium ions increased the cavity volume (Fig 4-D) but the impact is less pronounced. The distribution of water molecules around the magnesium ion was then slightly larger (Fig 4-F) and reequilibrated the population of bound magnesium ion in the cavity (Fig 4-E). Finally, the allosteric paths between SD2 and SD4 were also affected by the binding of ADP comprising fewer residues (Table S1). This resulted in shorter paths (Fig 4-G,H) mainly involving a direct interaction between ARG 62 and GLY 207 or passing through the TYR69-ARG183 interaction. Thus, for ADP binding, the actin was in a closed state and allosteric paths involved less the sensor loop for the correlation between SD2 and SD4 subdomains limiting the impact of histidine 73 methylation.

Impact of the K118N mutation on actin dynamics.

The K118N mutation is known to enhance actin polymerization and nucleation (***Ali et al., 2022***; ***Kruth and Rubenstein, 2012***). To understand the potential impact of this mutation on the actin dynamics, we performed simulations of this mutant in the presence of ATP or ADP. In the presence of ATP, the Cleft-dihedral map (Fig S1) revealed an actin conformation in a more open state ([-24°;26.5Å]) similar to conformations seen in the case of histidine methylation with addition of magnesium ions but locked around a specific minimum. In the presence of ADP, the mutation had a very low impact on the cleft-dihedral map. Thus, the K118N mutation favors a specific, open, conformation.

F-Actin plasticity at the barbed end.

We then studied the conformational dynamics of actin monomers at the extremity of a filament. We were especially interested by the barbed end, the most dynamic end, where ATP-G-actin monomers are primarily added (***Merino et al., 2020***). To do so, we performed simulations of a short filament containing four F-actin monomers whose the two last monomers at pointed end were constrained to mimic a longer filament (see details in the Method section). Each actin monomer contained the methylation of histidine 73 and were simulated with ATP or ADP. As done for the G-actin monomer systems, we carried out 1.52 µs long adaptive sampling polarizable molecular dynamics simulations. We assessed the dynamics of the last (B) and penultimate (B-1) monomers at the barbed end (Fig 5-A), which seem to experience major deformations (***Zsolnay et al., 2020***). Contrary to G-actin structure, the largest changes of the last F-actin monomer were observed for the binding of ADP while these changes were limited for ATP binding (Fig 5-A and Fig S6-A). Specifically, with ADP, the cleft-dihedral map displayed values tending to reach the ones observed for the G-actin monomers (Fig 4-B) while the B monomer stayed in a more flatten configuration when ATP nucleotide is bound. The B-1 subunit appeared to be less affected by the nucleotide state, probably due to a higher number of contacts with the other monomers in the filament (Fig S5, S6). Nevertheless, the B-1 subunit explored larger cleft distances in the ADP bound form than in the ATP bound form (Fig S5). For both B and B-1 subunits, the dynamics of the 220-230 helix (Fig 4-C) is the most affected (Fig S6). This helix from the B subunit strongly interacted with the C-terminal residues of the B-1 subunit for bound ADP but not in the case of bound ATP (Fig 4-D). This C-terminal part interacts with the D-loop of incoming actin monomer (***Durer et al., 2012***). Thus, the ADP bound actin may

compete with the D-loop from an approaching actin monomer delaying the filament elongation.

Discussion

Actin has been one of the most studied proteins by theoretical means over the last 20 years, in monomer (***Splettstoesser et al., 2009***; ***Saunders and Voth, 2011***; ***Saunders et al., 2014***; ***McCullagh et al., 2014***; ***Jepsen and Sept, 2020***) or in filament (***Chu and Voth, 2005***; ***Hocky et al., 2016***; ***Jepsen and Sept, 2020***; ***Zsolnay et al., 2020***). All of these theoretical works have been achieved using classical atomistic force fields with a fixed partial charge on each atom. The recent developments of Tinker-HP (***Lagardère et al., 2015***; ***Lipparini et al., 2014***; ***Lagardère et al., 2018***; ***Lagardère et al., 2019***; ***Adjoua et al., 2021***) has opened the door to study biological systems with polarizable force-field reaching simulations time up to several microseconds (***Jaffrelot Inizan et al., 2021***; ***El Ahdab et al., 2021***). In this study we have performed a series of adaptive sampling simulations using the AMOEBA polarizable force field on 12 different actin systems (Table 1), reaching a total of more than 18 µs of simulation. This demonstrated how it is now possible to study structural changes in large biomolecular systems using a polarizable force field. We focused our work on β-actin, an important isoform not yet studied by molecular dynamics simulations. Our results highlights the differences between α-actin and β-actin isoforms in term of dynamical behaviour (Fig S1) prompting us to further investigate this isoform.

The methylation of histidine 73, a post translational modification conserved in several animals (***Johnson et al., 1967***), has recently regained interest following the structure determination of the SETD3 methyltransferase (***Kwiatkowski et al., 2018***; ***Wilkinson et al., 2019***). Actin purified from Setd3 knockout shows an increased rate of nucleotide exchange and decreased polymerization kinetics (***Wilkinson et al., 2019***). Additionally, Setd3 knockout cells show a decrease in F-actin content, which is consistent with the prediction that methylation increases actin filament stability (***Kwiatkowski et al., 2018***). Our results showed an enhanced dynamics of the actin monomer once methylated, in the ATP state, in both α and β isoforms (Fig 1 and Fig S1). This resulted in the opening of the cleft due to the disruption of direct interactions between ARG 62 and GLU 207 respectively on SD2 and SD4 subdomains (Fig 2) which may help the structural adaptation of the actin monomer at the extremity of the filament. Furthermore, ARG 62 and GLU 207 residues are also involved in inter-monomer interactions in the filament (***Oda et al., 2009***). Thus, intra-monomer interactions may compete with inter-monomer interactions during the process of filament elongation and nucleation which may delay the formation of actin filament. Our results showed how breaking these interactions via the introduction of histidine methylation may thus explain an increase in actin filament nucleation. Our results also highlighted that without the histidine methylation the cavity volume is quite narrow and the number of water molecules in the cavity smaller (Fig 2-C,E). This can be related to the water network which may play an important role in the hydrolysis of the ATP (***McCullagh et al., 2014***). The histidine methylation may then modify the organisation of water molecules with an increase of cavity volume and number of water molecules (Fig 2-C,E) thus modulating the ATP hydrolysis, otherwise prematurely started in non-methylated actin (***Nyman et al., 2002***).

Previous works have shown how the magnesium ions concentration enhances actin polymerization (***Kang et al., 2012***). Here, the addition of magnesium ions enhanced the actin flexibility and increased the cleft distance for the ATP bound state with histidine methylation (Fig 1-B). This can further link the opening of the actin with its ability to adapt and interact with other actin subunits at the filament extremities. Interestingly, the K118N mutation, known to enhance actin polymerization (***Ali et al., 2022***), locked the actin structure in an open state (Fig S1, S2).

Actin protein seems less likely to polymerize in the presence of ADP (***Cooke, 1975***). Here, we have shown that the plasticity of the actin is drastically affected in the presence of ATP limiting the opening of the cleft for all the studied conditions (Fig 4-B). Thus ADP binding may lock the actin monomer in an closed state (Fig 4-G) which may prevent it from easily adapting its structure to elongate the filament. Furthermore, at the the barbed end, F-actin with ADP bound displayed

larger structural deformations towards a G-actin form while F-actin with ATP bound seemed more stable (Fig 5-B). Interestingly, the F-actin with ADP bound started interacting with the C-terminal part of the penultimate subunit (Fig 5-C,D) which may prevent the interaction of an incoming actin monomer via its D-loop (***Zsolnay et al., 2020***; ***Durer et al., 2012***). Thus, by stabilizing G-actin closed form and destabilizing F-actin form, the ADP may limit the polymerization of the actin filament.

Using correlation-based dynamical network analysis (Fig 3, Fig 4-G, and Fig S4) we were able to link actin flexibility with different paths between the SD2 and SD4 subdomains. Regarding the ATP-bound systems, these paths mainly involved the sensor loop in the open state. Conversely, paths observed in ADP bound states almost never involved this loop, minimizing the histidine methylation effects on SD2-SD4 mobility. Altogether, these may give a first clue on allosteric pathways linking molecular rearrangements in the binding site to large conformational changes at the actin extremities.

Taken together, our results highlight how the post translational modification of histidine 73 can change the dynamical properties of actin structure and can act in concert with other parameters such as the type of nucleotide and ions. By bridging changes at the molecular level to structural flexibility, these results highlight allosteric paths which may be targeted by ligands in order to create specfic allosteric modulators of the β-actin isoform.

Methods and Materials

Systems preparation

The initial structures of the Actin monomer in the ATP and ADP were obtained from the 1NWK(***Graceffa and Dominguez, 2003***) and 1J6Z(***Otterbein et al., 2001***) pdb files respectively. In the ATP state, the α and β-actin sequences were used. As the N-terminal acetylation or arginylation of the β-actin is known to have diverse biological effects (***Varland et al., 2019***; ***Chen and Kashina, 2021***), we decided to remove the N-terminal amino acid, starting our β-actin sequence at ASP2. The N-terminal and C-terminal extremities and the D-loop were generated using modeller(***Šali and Blundell, 1993***). In the original pdb files, the nucleotide is under the form of AMP and in presence of a calcium ion. We morphed the AMP into ATP and replaced the calcium ion for a magnesium ion, to stick closer to physiological conditions. It has been demonstrated that crystallographic water molecules located inside the cavity may impact the behaviour of the protein(***Saunders and Voth, 2011***). Therefore, the water molecules placed at less than 10Åof the magnesium ion were kept at the start of the simulation. In addition to the monomer systems, two 4-mer systems were prepared based on the 6BNO(***Gurel et al., 2017***) pdb file, in presence of ADP and ATP. For the ATP state, the ADP has been morphed into ATP. The N-terminal and C-terminal extremities only were generated using modeller. For all systems, the residues have been protonated following the results of PROPKA3(***Olsson et al., 2011***). All systems were solvated in water boxes using the xyzedit tool of the Tinker-hp distribution(***Rackers et al., 2018***), so that there was at least 20Åbetween two images of the protein. The systems were then neutralized and KCL atoms were added to reach 150mM concentration. Regarding the simulations at high MG2+ ions concentrations, all K+ atoms were replaced by half number of MG2+ ions. The force field parameters used for the protein parameters was the AMOEBA Polarizable force field for proteins(***Shi et al., 2013***). Previously published parameters were used for the ATP and ADP systems(***Walker et al., 2020***). The parameters of the HIC73 residues were developed following the procedure used to develop the AMOEBA force field for proteins. All QM calculations were performed using Gaussian09(***Frisch et al., 2009***). The model residue used to develop the parameters was a dipeptide Ac-HIC-NME were the Ac, NME and backbone parameters were extracted from the AMOEBABIO18 force field(citep amoeba nucleic acids). Briefly, geometry optimisation were carried out at the MP2/6-31G* level. Initial atomic multipoles were derived at the MP2/6-311G** level using the Distributed Dipole Analysis (DMA) procedure(***Stone, 1981***). The resulting atomic multipôles were optimized against MP2/aug-cc-pvtz electrostatic potential on a set of grid points distributed around the dipeptide. During this fitting, the monopoles were held fixed.

The point charges were adjusted at the junction atom between the backbone and the sidechain (adjustment of 0.03 on the -CH2- carbon atom charge), to insure electrical neutrality. As realised in the original AMOEBA for protein publication, 3 conformations were used to realize the fitting of the dipôle and multipôle components. The valence,vdW and torsional parameters were extracted from the AMOEBA parameters of the classical HIS residue.

Simulation setup

All molecular dynamics simulations were performed using the GPU version of the Tinker-HP software(***Adjoua et al., 2021***). During the calculations, periodic boundary conditions were employed using the Particle Mesh Ewald method. The van der Walls and PME cutoffs were respectively of 12Åand 7Å. An analytical long range correction of the vdW parameters has been used. The dipole convergence criterion of the preconditioned conjugate gradient polarization solver was set up to 0.01 Debye/atom for the minimization steps, and to 0.00001 Debye/atom otherwise. For the minimization steps, no polarization or multipole terms were used. The systems underwent a minimization of 30 000 step using the steepest descent algorithm. The next equilibration steps were realised by using a timestep of 1fs, the RESPA propagator and the berendsen barostat (when relevant) unless stated otherwise. The solvent was then progressively heat up in the NVT ensemble, coming from 5K to 300K using 10K steps and spending 5ps at each temperature, before undergoing additional 100ps at 300K. The system was then allow to slowly relax 3x 400ps in the NPT ensemble while applying harmonic constraints 10, 5 and finally 1 kcal/mol on the backbone atoms of the protein. At this point, all restraints were removed from the systems, and we used the montecarlo barostat in combination with the BAOAB-RESPA1(***Lagardère et al., 2019***) propagator. Three final equilibration steps were performed during 100ps, 200ps and 500 ps by respectively increasing the outer timestep from 1fs to 2s, then 5fs. Regarding the production run, all calculations were performed in the NPT ensemble, using the montecarlo barostat and the BAOAB-RESPA1 propagator with an outer timestep of 5fs, and hydrogen mass repartioning. A first 10ns simulations was performed to generate a first set of structures. In order to maximize the space exploration on our system, we then realized a procedural adaptive sampling procedure: a certain number of structures were first extracted from this initial simulation to perform the first adaptive sampling round. The seeds are chosen following a procedure already described(***Jaffrelot Inizan et al., 2021***). Briefly, a principal component analysis is performed on the 10ns simulation using the scikit-learn(***Pedregosa et al., 2011***) and MDTraj(***McGibbon et al., 2015***) packages from which the n=4 first principal modes are considered (note:10 modes are calculated). The density ρ_k of the collective variables is then projected on the 4 modes and approximated using a Gaussian density kernel estimator:

$$\rho_k(x_i) = \frac{1}{(2\pi\sigma^2)^{n/2} M_k} \sum_{i=1}^{M_k} \exp - \frac{|x - x_i|^2}{2\sigma^2} \tag{1}$$

With the σ bandwith being chosen with the D.W Scott method of Scipy(***Virtanen et al., 2020***), M_k being the total number of configurations, x_i the orthogonal projection of the configuration on the n PCA modes. Then a bias is introduced to the selection of a new seed x_i under the following form :

$$P(i) = \frac{\rho_k^{-1}(x_i)}{\sum_{j=1}^{M_k} \rho_k^{-1}(x_j)} \tag{2}$$

The probability of selecting the x_i structure is inversely proportional to its density, projected on the first 4 PCA components. This allows to equalize the chances of selecting rare structures as well as highly present ones, allowing to search for new, undiscovered structural states. Following this, 10 ns simulations are set up and will form the new space of structures for the next adaptive sampling round. For each following round, all simulations will be added to the space of structured

Table 2. Number of seeds of each round of Adaptive sampling.

1st	2nd to 10th	total simulation time
8*10ns	16*10ns	1.52µs

Table 3. Definition of each subdomain

	SD1	SD2	SD3	SD4
Residues	5-33 80-147 334-349	34-39 52-69	148-179 273-333	180-219 252-262

on which the next adaptive sampling will be performed. The number of seeds used on each round is summed in Table 2. Regarding the 4-mer systems, we were interested in the behaviour of the barbed end only. For this extremity, it has recently been demonstrated that the behaviour of the B and B-1 residues is different of other residues of the filament. Therefore, to simulate the behaviour of this extremity only, the backbone atoms of two monomers forming the pointed end have been constrained using a 10kcal/mol restraint. This way, it was possible to study the evolution of the barbed end in a constrained filament, while keeping the sidechains free. Finally, 1.52 µs long simulations were generated on eight monomer systems and two 4-mer systems, resulting in a total of 18.24 µs.

Analysis

Most quantities has been calculated using the VMD software(***Humphrey et al., 1996***). Regarding the cavity, volumes have been computed with E-pock(***Laurent et al., 2015***). Finally, shortest paths have been calculated using the Dynetan tool(***Melo et al., 2020***). Each of the observable had to be reweighted to take into account the bias introduced by the adaptive sampling. For this purpose, the unbiasing factor α_i of each seed is defined as :

$$\alpha_i = \frac{1}{M_k P(i)} \tag{3}$$

The final weight of each seed is then :

$$\omega_i = \frac{\alpha_i}{\sum_j \alpha_j} \tag{4}$$

The dihedral and cleft angle has been defined following the work of Saunders and coworkers(***Saunders et al., 2014***): Dihedral = SD2-SD1-SD3-SD4, Cleft = SD2-SD4 distance. To compute these quantities, the center of mass of each subdomains have been defined as following:

The volume of the cavity has been calculated by defining a 6Åsphere around the N1, N9, PA, PG (PB for ADP) atoms of the nucleotide and one additional sphere around the MG2+ ion coordinated to it. For the calculation of shortest paths, the shortest path of each seed has been calculated on the 10ns. Then all found shortest paths were reweighted accross all seeds, and the 3 highest shortest paths have been kept for figures. All shortest paths accounting for more than 3 percent of all paths are available in supplementary informations.

Acknowledgments

A. D. is funded by the ITMO Cancer of Aviesan "Mathematiques et Informatique". This work has also received funding from the European Research Council (ERC) under the European Union's Horizon 2020 research and innovation program (grant agreement No 810367), project EMC2 (JPP). This work was granted access to the HPC resources of CALMIP supercomputing center (under the allocation 2021-P21020) and TGCC Joliot-Curie supercomputer (under the GENCI allocation A0110712941).

References

Adjoua O, Lagardère L, Jolly LH, Durocher A, Very T, Dupays I, Wang Z, Inizan TJ, Célerse F, Ren P, Ponder JW, Piquemal JP. Tinker-HP: Accelerating Molecular Dynamics Simulations of Large Complex Systems with Advanced Point Dipole Polarizable Force Fields Using GPUs and Multi-GPU Systems. Journal of Chemical Theory and Computation. 2021; 17(4):2034–2053. doi: 10.1021/acs.jctc.0c01164.

Ali R, Zahm JA, Rosen MK. Bound nucleotide can control the dynamic architecture of monomeric actin. Nature Structural & Molecular Biology. 2022 Apr; 29(4):320–328. https://doi.org/10.1038/s41594-022-00743-5, doi: 10.1038/s41594-022-00743-5.

Bellissent-Funel MC, Hassanali A, Havenith M, Henchman R, Pohl P, Sterpone F, van der Spoel D, Xu Y, Garcia AE. Water Determines the Structure and Dynamics of Proteins. Chemical Reviews. 2016; 116(13):7673–7697. https://doi.org/10.1021/acs.chemrev.5b00664, doi: 10.1021/acs.chemrev.5b00664, pMID: 27186992.

Blanchoin L, Pollard TD. Hydrolysis of ATP by Polymerized Actin Depends on the Bound Divalent Cation but Not Profilin. Biochemistry. 2002 Jan; 41(2):597–602. https://doi.org/10.1021/bi011214b, doi: 10.1021/bi011214b.

Bowman GR, Ensign DL, Pande VS. Enhanced Modeling via Network Theory: Adaptive Sampling of Markov State Models. Journal of Chemical Theory and Computation. 2010; 6(3):787–794. https://doi.org/10.1021/ct900620b, doi: 10.1021/ct900620b, pMID: 23626502.

Castaneda N, Lee M, Rivera-Jacquez HJ, Marracino RR, Merlino TR, Kang H. Actin Filament Mechanics and Structure in Crowded Environments. The Journal of Physical Chemistry B. 2019; 123(13):2770–2779. https://doi.org/10.1021/acs.jpcb.8b12320, doi: 10.1021/acs.jpcb.8b12320, pMID: 30817154.

Chen L, Kashina A. Post-translational Modifications of the Protein Termini. Frontiers in Cell and Developmental Biology. 2021; 9. https://www.frontiersin.org/articles/10.3389/fcell.2021.719590, doi: 10.3389/fcell.2021.719590.

Chu JW, Voth GA. Allostery of actin filaments: Molecular dynamics simulations and coarse-grained analysis. Proceedings of the National Academy of Sciences. 2005; 102(37):13111–13116. https://www.pnas.org/doi/abs/10.1073/pnas.0503732102, doi: 10.1073/pnas.0503732102.

Cooke R. Role of the bound nucleotide in the polymerization of actin. Biochemistry. 1975; 14(14):3250–3256. https://doi.org/10.1021/bi00685a035, doi: 10.1021/bi00685a035, pMID: 1148203.

Célerse F, Inizan TJ, Lagardère L, Adjoua O, Monmarché P, Miao Y, Derat E, Piquemal JP. An Efficient Gaussian-Accelerated Molecular Dynamics (GaMD) Multilevel Enhanced Sampling Strategy: Application to Polarizable Force Fields Simulations of Large Biological Systems. Journal of Chemical Theory and Computation. 2022; 18(2):968–977. doi: 10.1021/acs.jctc.1c01024, pMID: 35080892.

Célerse F, Lagardère L, Derat E, Piquemal JP. Massively Parallel Implementation of Steered Molecular Dynamics in Tinker-HP: Comparisons of Polarizable and Non-Polarizable Simulations of Realistic Systems. Journal of Chemical Theory and Computation. 2019; 15(6):3694–3709. https://doi.org/10.1021/acs.jctc.9b00199, doi: 10.1021/acs.jctc.9b00199, pMID: 31059250.

Durer Z, Kudryashov D, Sawaya M, Altenbach C, Hubbell W, Reisler E. Structural States and Dynamics of the D-Loop in Actin. Biophysical Journal. 2012; 103(5):930–939. https://www.sciencedirect.com/science/article/pii/S0006349512008065, doi: https://doi.org/10.1016/j.bpj.2012.07.030.

El Ahdab D, Lagardère L, Inizan TJ, Célerse F, Liu C, Adjoua O, Jolly LH, Gresh N, Hobaika Z, Ren P, Maroun RG, Piquemal JP. Interfacial Water Many-Body Effects Drive Structural Dynamics and Allosteric Interactions in SARS-CoV-2 Main Protease Dimerization Interface. The Journal of Physical Chemistry Letters. 2021; 12(26):6218–6226. doi: 10.1021/acs.jpclett.1c01460, pMID: 34196568.

El Khoury L, Jing Z, Cuzzolin A, Deplano A, Loco D, Sattarov B, Hédin F, Wendeborn S, Ho C, El Ahdab D, Jaffrelot Inizan T, Sturlese M, Sosic A, Volpiana M, Lugato A, Barone M, Gatto B, Macchia ML, Bellanda M, Battistutta R, et al. Computationally driven discovery of SARS-CoV-2 Mpro inhibitors: from design to experimental validation. Chem Sci. 2022; 13:3674–3687. http://dx.doi.org/10.1039/D1SC05892D, doi: 10.1039/D1SC05892D.

Frisch MJ, Trucks GW, Schlegel HB, Scuseria GE, Robb MA, Cheeseman JR, Scalmani G, Barone V, Mennucci B, Petersson GA, Nakatsuji H, Caricato M, Li X, Hratchian HP, Izmaylov AF, Bloino J, Zheng G, Sonnenberg JL, Hada M, Ehara M, et al., Gaussian 09 Revision A.2; 2009.

Graceffa P, Dominguez R. Crystal structure of monomeric actin in the ATP state: Structural basis of nucleotide-dependent actin dynamics. Journal of Biological Chemistry. 2003; 278(36):34172–34180. http://dx.doi.org/10.1074/jbc.M303689200, doi: 10.1074/jbc.M303689200.

Gurel PS, Kim LY, Ruijgrok PV, Omabegho T, Bryant Z, Alushin GM. Cryo-EM structures reveal specialization at the myosin VI-actin interface and a mechanism of force sensitivity. eLife. 2017; 6(Md):1–33. doi: 10.7554/eLife.31125.

Helal MA, Khalifa S, Ahmed S. Differential Binding of Latrunculins to G-Actin: A Molecular Dynamics Study. Journal of Chemical Information and Modeling. 2013; 53(9):2369–2375. https://doi.org/10.1021/ci400317j, doi: 10.1021/ci400317j, pMID: 23988111.

Hocky GM, Baker JL, Bradley MJ, Sinitskiy AV, De La Cruz EM, Voth GA. Cations Stiffen Actin Filaments by Adhering a Key Structural Element to Adjacent Subunits. The Journal of Physical Chemistry B. 2016; 120(20):4558–4567. https://doi.org/10.1021/acs.jpcb.6b02741, doi: 10.1021/acs.jpcb.6b02741, pMID: 27146246.

Horan BG, Hall AR, Vavylonis D. Insights into Actin Polymerization and Nucleation Using a Coarse-Grained Model. Biophysical Journal. 2020; 119(3):553–566. https://www.sciencedirect.com/science/article/pii/S0006349520304951, doi: https://doi.org/10.1016/j.bpj.2020.06.019.

Humphrey W, Dalke A, Schulten K. VMD: Visual Molecular Dynamics. Journal of molecular graphics. 1996; 14(October 1995):33–38. https://www.tapbiosystems.com/tap/products/index.htm.

Jaffrelot Inizan T, Célerse F, Adjoua O, El Ahdab D, Jolly LH, Liu C, Ren P, Montes M, Lagarde N, Lagardère L, Monmarché P, Piquemal JP. High-resolution mining of the SARS-CoV-2 main protease conformational space: supercomputer-driven unsupervised adaptive sampling. Chemical Science. 2021; 12(2003). doi: 10.1039/d1sc00145k.

Jaswandkar SV, Faisal HMN, Katti KS, Katti DR. Dissociation Mechanisms of G-actin Subunits Govern Deformation Response of Actin Filament. Biomacromolecules. 2021; 22(2):907–917. https://doi.org/10.1021/acs.biomac.0c01602, doi: 10.1021/acs.biomac.0c01602, pMID: 33481563.

Jepsen L, Sept D. Effects of Nucleotide and End-Dependent Actin Conformations on Polymerization. Biophysical Journal. 2020; 119(9):1800–1810. https://www.sciencedirect.com/science/article/pii/S0006349520307359, doi: https://doi.org/10.1016/j.bpj.2020.09.024.

Jing Z, Liu C, Cheng SY, Qi R, Walker BD, Piquemal JP, Ren P. Polarizable Force Fields for Biomolecular Simulations: Recent Advances and Applications. Annu Rev Biophys. 2019 Mar; 48:371–394.

Jing Z, Rackers JA, Pratt LR, Liu C, Rempe SB, Ren P. Thermodynamics of ion binding and occupancy in potassium channels. Chem Sci. 2021; 12:8920–8930. http://dx.doi.org/10.1039/D1SC01887F, doi: 10.1039/D1SC01887F.

Johnson P, Harris CI, Perry SV. 3-Methylhistidine in actin and other muscle proteins. Biochemical Journal. 1967 10; 105(1):361–370. https://doi.org/10.1042/bj1050361, doi: 10.1042/bj1050361.

Kadaoluwa Pathirannahalage SP, Meftahi N, Elbourne A, Weiss ACG, McConville CF, Padua A, Winkler DA, Costa Gomes M, Greaves TL, Le TC, Besford QA, Christofferson AJ. Systematic Comparison of the Structural and Dynamic Properties of Commonly Used Water Models for Molecular Dynamics Simulations. Journal of Chemical Information and Modeling. 2021; 61(9):4521–4536. https://doi.org/10.1021/acs.jcim.1c00794, doi: 10.1021/acs.jcim.1c00794, pMID: 34406000.

Kang H, Bradley MJ, McCullough BR, Pierre A, Grintsevich EE, Reisler E, Cruz EMDL. Identification of cation-binding sites on actin that drive polymerization and modulate bending stiffness. Proceedings of the National Academy of Sciences. 2012; 109(42):16923–16927. https://www.pnas.org/doi/abs/10.1073/pnas.1211078109, doi: 10.1073/pnas.1211078109.

Kang H, Bradley M, Elam W, De La Cruz E. Regulation of Actin by Ion-Linked Equilibria. Biophysical Journal. 2013; 105(12):2621–2628. https://www.sciencedirect.com/science/article/pii/S0006349513012009, doi: https://doi.org/10.1016/j.bpj.2013.10.032.

Kim YC, Hummer G. Coarse-grained Models for Simulations of Multiprotein Complexes: Application to Ubiquitin Binding. Journal of Molecular Biology. 2008; 375(5):1416–1433. https://www.sciencedirect.com/science/article/pii/S0022283607015628, doi: https://doi.org/10.1016/j.jmb.2007.11.063.

Kopec W, Köpfer DA, Vickery ON, Bondarenko AS, Jansen TLC, de Groot BL, Zachariae U. Direct knock-on of desolvated ions governs strict ion selectivity in K+ channels. Nature Chemistry. 2018 Aug; 10(8):813–820. https://doi.org/10.1038/s41557-018-0105-9, doi: 10.1038/s41557-018-0105-9.

Kratochvil HT, Carr JK, Matulef K, Annen AW, Li H, Maj M, Ostmeyer J, Serrano AL, Raghuraman H, Moran SD, Skinner JL, Perozo E, Roux B, Valiyaveetil FI, Zanni MT. Instantaneous ion configurations in the K⁺ ion channel selectivity filter revealed by 2D IR spectroscopy. Science. 2016; 353(6303):1040–1044. https://www.science.org/doi/abs/10.1126/science.aag1447, doi: 10.1126/science.aag1447.

Kruth KA, Rubenstein PA. Two Deafness-causing (DFNA20/26) Actin Mutations Affect Arp2/3-dependent Actin Regulation*. Journal of Biological Chemistry. 2012; 287(32):27217–27226. https://www.sciencedirect.com/science/article/pii/S0021925820479190, doi: https://doi.org/10.1074/jbc.M112.377283.

Kwiatkowski S, Seliga AK, Vertommen D, Terreri M, Ishikawa T, Grabowska I, Tiebe M, Teleman AA, Jagielski AK, Veiga-Da-Cunha M, Drozak J. SETD3 protein is the actin-specific histidine N-methyltransferase. eLife. 2018; 7(2016):1–42. doi: 10.7554/eLife.37921.

Lagardère L, Aviat F, Piquemal JP. Pushing the Limits of Multiple-Time-Step Strategies for Polarizable Point Dipole Molecular Dynamics. Journal of Physical Chemistry Letters. 2019; 10(10):2593–2599. doi: 10.1021/acs.jpclett.9b00901.

Lagardère L, Lipparini F, Polack É, Stamm B, Cancès É, Schnieders M, Ren P, Maday Y, Piquemal JP. Scalable Evaluation of Polarization Energy and Associated Forces in Polarizable Molecular Dynamics: II. Toward Massively Parallel Computations Using Smooth Particle Mesh Ewald. Journal of Chemical Theory and Computation. 2015; 11(6):2589–2599. doi: 10.1021/acs.jctc.5b00171.

Lagardère L, Jolly LH, Lipparini F, Aviat F, Stamm B, Jing ZF, Harger M, Torabifard H, Cisneros GA, Schnieders MJ, Gresh N, Maday Y, Ren PY, Ponder JW, Piquemal JP. Tinker-HP: a massively parallel molecular dynamics package for multiscale simulations of large complex systems with advanced point dipole polarizable force fields. Chem Sci. 2018; 9:956–972. http://dx.doi.org/10.1039/C7SC04531J, doi: 10.1039/C7SC04531J.

Laurent B, Chavent M, Cragnolini T, Dahl ACE, Pasquali S, Derreumaux P, Sansom MSP, Baaden M. Epock: Rapid analysis of protein pocket dynamics. Bioinformatics. 2015; 31(9):1478–1480. doi: 10.1093/bioinformatics/btu822.

Li H, Ngo V, Silva MCD, Salahub DR, Callahan K, Roux B, Noskov SY. Representation of Ion–Protein Interactions Using the Drude Polarizable Force-Field. The Journal of Physical Chemistry B. 2015; 119(29):9401–9416. doi: 10.1021/jp510560k.

Lipparini F, Lagardère L, Stamm B, Cancès É, Schnieders M, Ren P, Maday Y, Piquemal JP. Scalable Evaluation of Polarization Energy and Associated Forces in Polarizable Molecular Dynamics: II. Toward Massively Parallel Computations Using Smooth Particle Mesh Ewald. Journal of Chemical Theory and Computation. 2014; 10(6):1638–1651. doi: 10.1021/acs.jctc.5b00171.

Lynch CI, Klesse G, Rao S, Tucker SJ, Sansom MSP. Water Nanoconfined in a Hydrophobic Pore: Molecular Dynamics Simulations of Transmembrane Protein 175 and the Influence of Water Models. ACS Nano. 2021; 15(12):19098–19108. https://doi.org/10.1021/acsnano.1c06443, doi: 10.1021/acsnano.1c06443, pMID: 34784172.

Maier JA, Martinez C, Kasavajhala K, Wickstrom L, Hauser KE, Simmerling C. ff14SB: Improving the Accuracy of Protein Side Chain and Backbone Parameters from ff99SB. Journal of Chemical Theory and Computation. 2015; 11(8):3696–3713. https://doi.org/10.1021/acs.jctc.5b00255, doi: 10.1021/acs.jctc.5b00255, pMID: 26574453.

McCullagh M, Saunders MG, Voth GA. Unraveling the Mystery of ATP Hydrolysis in Actin Filaments. Journal of the American Chemical Society. 2014; 136(37):13053–13058. https://doi.org/10.1021/ja507169f, doi: 10.1021/ja507169f, pMID: 25181471.

McGibbon RT, Beauchamp KA, Harrigan MP, Klein C, Swails JM, Hernández CX, Schwantes CR, Wang LP, Lane TJ, Pande VS. MDTraj: A Modern Open Library for the Analysis of Molecular Dynamics Trajectories. Biophysical Journal. 2015; 109(8):1528–1532. doi: 10.1016/j.bpj.2015.08.015.

Melcr J, Piquemal JP. Accurate Biomolecular Simulations Account for Electronic Polarization. Frontiers in Molecular Biosciences. 2019 Dec; 6. https://doi.org/10.3389/fmolb.2019.00143, doi: 10.3389/fmolb.2019.00143.

Melo MCR, Bernardi RC, De La Fuente-Nunez C, Luthey-Schulten Z. Generalized correlation-based dynamical network analysis: A new high-performance approach for identifying allosteric communications in molecular dynamics trajectories. Journal of Chemical Physics. 2020; 153(13). https://doi.org/10.1063/5.0018980, doi: 10.1063/5.0018980.

Merino F, Pospich S, Raunser S. Towards a structural understanding of the remodeling of the actin cytoskeleton. Seminars in Cell & Developmental Biology. 2020; 102:51–64. https://www.sciencedirect.com/science/article/pii/S1084952119301909, doi: https://doi.org/10.1016/j.semcdb.2019.11.018, sI: $Actin_15$ June 2019.

Miao Y, Feher VA, McCammon JA. Gaussian Accelerated Molecular Dynamics: Unconstrained Enhanced Sampling and Free Energy Calculation. Journal of Chemical Theory and Computation. 2015; 11(8):3584–3595. https://doi.org/10.1021/acs.jctc.5b00436, doi: 10.1021/acs.jctc.5b00436, pMID: 26300708.

Nyman T, Schüler H, Korenbaum E, Schutt CE, Karlsson R, Lindberg U. The role of MeH73 in actin polymerization and ATP hydrolysis. Journal of Molecular Biology. 2002; 317(4):577–589. https://www.sciencedirect.com/science/article/pii/S0022283602954367, doi: https://doi.org/10.1006/jmbi.2002.5436.

Oda T, Iwasa M, Aihara T, Maéda Y, Narita A. The nature of the globular- to fibrous-actin transition. Nature. 2009 Jan; 457(7228):441–445. https://doi.org/10.1038/nature07685, doi: 10.1038/nature07685.

Olsson MHM, SØndergaard CR, Rostkowski M, Jensen JH. PROPKA3: Consistent treatment of internal and surface residues in empirical p K a predictions. Journal of Chemical Theory and Computation. 2011; 7(2):525–537. doi: 10.1021/ct100578z.

Otterbein LR, Graceffa P, Dominguez R. The crystal structure of uncomplexed actin in the ADP state. Science. 2001; 293(5530):708–711. doi: 10.1126/science.1059700.

Pedregosa F, Varoquaux G, Gramfort A, Michel V, Thirion B, Grisel O, Blondel M, Prettenhofer P, Weiss R, Dubourg V, Vanderplas J, Passos A, Cournapeau D, Brucher M, Perrot M, Duchesnay E. Scikit-learn: Machine Learning in Python. JMLR. 2011; 12(82):2825–2830.

Perrin BJ, Ervasti JM. The actin gene family: Function follows isoform. Cytoskeleton. 2010; 67(10):630–634. doi: 10.1002/cm.20475.

Rackers JA, Wang Z, Lu C, Laury ML, Lagardère L, Schnieders MJ, Piquemal JP, Ren P, Ponder JW. Tinker 8: Software Tools for Molecular Design. Journal of Chemical Theory and Computation. 2018; 14(10):5273–5289. doi: 10.1021/acs.jctc.8b00529.

Rennebaum S, Caflisch A. Inhibition of interdomain motion in g-actin by the natural product latrunculin: A molecular dynamics study. Proteins: Structure, Function, and Bioinformatics. 2012; 80(8):1998–2008. https://onlinelibrary.wiley.com/doi/abs/10.1002/prot.24088, doi: https://doi.org/10.1002/prot.24088.

Reynolds MJ, Hachicho C, Carl AG, Gong R, Alushin GM. Bending forces and nucleotide state jointly regulate F-actin structure. Nature. 2022; 611:380–386. doi: 10.1038/s41586-022-05366-w.

Šali A, Blundell TL, Comparative Protein Modelling by Satisfaction of Spatial Restraints; 1993.

Saunders MG, Tempkin J, Weare J, Dinner AR, Roux B, Voth GA. Nucleotide regulation of the structure and dynamics of G-actin. Biophysical Journal. 2014; 106(8):1710–1720. doi: 10.1016/j.bpj.2014.03.012.

Saunders MG, Voth GA. Water molecules in the nucleotide binding cleft of actin: Effects on subunit conformation and implications for ATP hydrolysis. Journal of Molecular Biology. 2011; 413(1):279–291. http://dx.doi.org/10.1016/j.jmb.2011.07.068, doi: 10.1016/j.jmb.2011.07.068.

Schroer CFE, Baldauf L, van Buren L, Wassenaar TA, Melo MN, Koenderink GH, Marrink SJ. Charge-dependent interactions of monomeric and filamentous actin with lipid bilayers. Proceedings of the National Academy of Sciences. 2020; 117(11):5861–5872. https://www.pnas.org/doi/abs/10.1073/pnas.1914884117, doi: 10.1073/pnas.1914884117.

Shamloo A, Mehrafrooz B. Nanomechanics of actin filament: A molecular dynamics simulation. Cytoskeleton. 2018; 75(3):118–130. https://onlinelibrary.wiley.com/doi/abs/10.1002/cm.21429, doi: https://doi.org/10.1002/cm.21429.

Shi Y, Ren P, Schnieders M, Piquemal JP. 2. In: Polarizable Force Fields for Biomolecular Modeling John Wiley & Sons, Ltd; 2015. p. 51–86. https://onlinelibrary.wiley.com/doi/abs/10.1002/9781118889886.ch2, doi: https://doi.org/10.1002/9781118889886.ch2.

Shi Y, Xia Z, Zhang J, Best R, Wu C, Ponder JW, Ren P. Polarizable atomic multipole-based AMOEBA force field for proteins. Journal of Chemical Theory and Computation. 2013; 9(9):4046–4063. doi: 10.1021/ct4003702.

Song C, Weichbrodt C, Salnikov ES, Dynowski M, Forsberg BO, Bechinger B, Steinem C, de Groot BL, Zachariae U, Zeth K. Crystal structure and functional mechanism of a human antimicrobial membrane channel. Proceedings of the National Academy of Sciences. 2013; 110(12):4586–4591. https://www.pnas.org/doi/abs/10.1073/pnas.1214739110, doi: 10.1073/pnas.1214739110.

Souza PCT, Alessandri R, Barnoud J, Thallmair S, Faustino I, Grünewald F, Patmanidis I, Abdizadeh H, Bruininks BMH, Wassenaar TA, Kroon PC, Melcr J, Nieto V, Corradi V, Khan HM, Domański J, Javanainen M, Martinez-Seara H, Reuter N, Best RB, et al. Martini 3: a general purpose force field for coarse-grained molecular dynamics. Nature Methods. 2021 Apr; 18(4):382–388. https://doi.org/10.1038/s41592-021-01098-3, doi: 10.1038/s41592-021-01098-3.

Splettstoesser T, Holmes KC, Noé F, Smith JC. Structural modeling and molecular dynamics simulation of the actin filament. Proteins: Structure, Function, and Bioinformatics. 2011; 79(7):2033–2043. https://onlinelibrary.wiley.com/doi/abs/10.1002/prot.23017, doi: https://doi.org/10.1002/prot.23017.

Splettstoesser T, Noé F, Oda T, Smith JC. Nucleotide-dependence of G-actin conformation from multiple molecular dynamics simulations and observation of a putatively polymerization-competent superclosed state. Proteins: Structure, Function, and Bioinformatics. 2009; 76(2):353–364. https://onlinelibrary.wiley.com/doi/abs/10.1002/prot.22350, doi: https://doi.org/10.1002/prot.22350.

Stone AJ. Distributed multipole analysis, or how to describe a molecular charge distribution. Chemical Physics Letters. 1981; 83(2):233–239. doi: 10.1016/0009-2614(81)85452-8.

Svitkina T. The Actin Cytoskeleton and Actin-Based Motility. Cold Spring Harbor Perspectives in Biology. 2018; 10(1):a018267. doi: 10.1101/cshperspect.a018267.

Vanommeslaeghe K, Hatcher E, Acharya C, Kundu S, Zhong S, Shim J, Darian E, Guvench O, Lopes P, Vorobyov I, Mackerell Jr AD. CHARMM general force field: A force field for drug-like molecules compatible with the CHARMM all-atom additive biological force fields. Journal of Computational Chemistry. 2010; 31(4):671–690. https://onlinelibrary.wiley.com/doi/abs/10.1002/jcc.21367, doi: https://doi.org/10.1002/jcc.21367.

Varland S, Vandekerckhove J, Drazic A. Actin Post-translational Modifications: The Cinderella of Cytoskeletal Control. Trends in Biochemical Sciences. 2019; 44(6):502–516. https://doi.org/10.1016/j.tibs.2018.11.010, doi: 10.1016/j.tibs.2018.11.010.

Virtanen P, Gommers R, Oliphant TE, Haberland M, Reddy T, Cournapeau D, Burovski E, Peterson P, Weckesser W, Bright J, van der Walt SJ, Brett M, Wilson J, Millman KJ, Mayorov N, Nelson ARJ, Jones E, Kern R, Larson E, Carey CJ, et al. SciPy 1.0: fundamental algorithms for scientific computing in Python. Nature Methods. 2020; 17(3):261–272. doi: 10.1038/s41592-019-0686-2.

Walker B, Jing Z, Ren P. Molecular dynamics free energy simulations of ATP:Mg2+ and ADP:Mg2+ using the polarisable force field AMOEBA. Molecular Simulation. 2020; 0(0):1–10. https://doi.org/10.1080/08927022.2020.1725003, doi: 10.1080/08927022.2020.1725003.

Wegner A. Treadmilling of actin at physiological salt concentrations: An analysis of the critical concentrations of actin filaments. Journal of Molecular Biology. 1982; 161(4):607–615. https://www.sciencedirect.com/science/article/pii/0022283682904119, doi: https://doi.org/10.1016/0022-2836(82)90411-9.

Westerlund AM, Fleetwood O, Pérez-Conesa S, Delemotte L. Network analysis reveals how lipids and other cofactors influence membrane protein allostery. J Chem Phys. 2020 Oct; 153(14):141103.

Wilkinson AW, Diep J, Dai S, Liu S, Ooi YS, Song D, Li TM, Horton JR, Zhang X, Liu C, Trivedi DV, Ruppel KM, Vilches-Moure JG, Casey KM, Mak J, Cowan T, Elias JE, Nagamine CM, Spudich JA, Cheng X, et al. SETD3 is an actin histidine methyltransferase that prevents primary dystocia. Nature. 2019; 565(7739):372–376. http://dx.doi.org/10.1038/s41586-018-0821-8, doi: 10.1038/s41586-018-0821-8.

Zsolnay V, Katkar HH, Chou SZ, Pollard TD, Voth GA. Structural basis for polarized elongation of actin filaments. Proceedings of the National Academy of Sciences of the United States of America. 2020; 117(48):30458–30464. doi: 10.1073/pnas.2011128117.

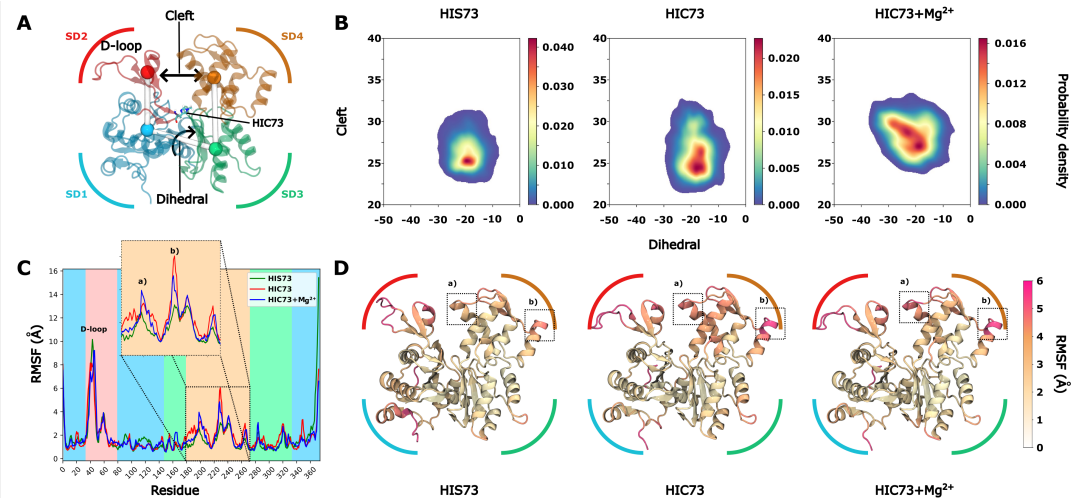

Figure 1. ATP-bound β-actin fluctuations. A- Subdomains localisation. Definition of the cleft as the distance between SD2 and SD4 and the dihedral angle formed by SD2-SD1-SD3-SD4 subdomains. **B-** Distribution of cleft-dihedrals for actin without methylation (HIS73), or with methylation (HIC73) in presence of KCl and $MgCl_2$ (HIC73+Mg). **C-** RMSF of each system. Zoom on the SD4 subdomain, with a focus on a) [200-206] and b) [228-232] helices **D-** Representation of each system colored according to their RMSF.

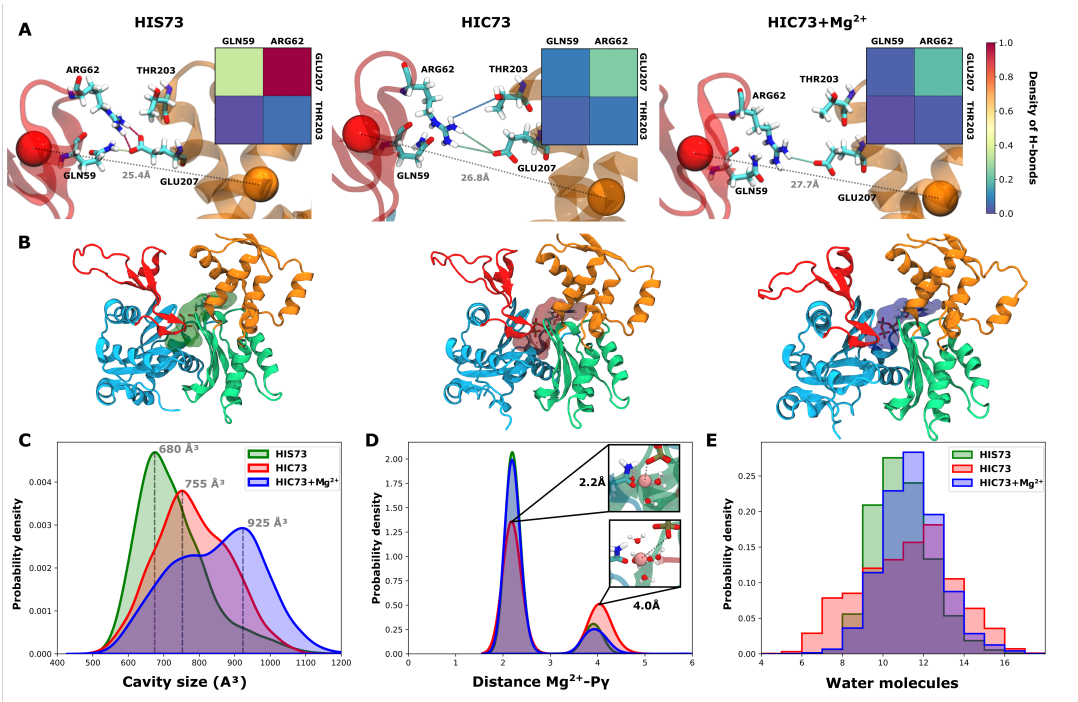

Figure 2. Local variations of ATP-bound β-actin systems A- Representation of main links involving SD2 and SD4 residues. Links are colored with respect to the normalized density of Hbonds between these residues along simulations. **B-** Representation of nucleotide cavity located in main basin of fig 1. **C-** Cavity size of each system **D-** Distance between magnesium Ion and γ-phosphate. **E-** Number of water molecules located at 5Å or less of the magnesium Ion.

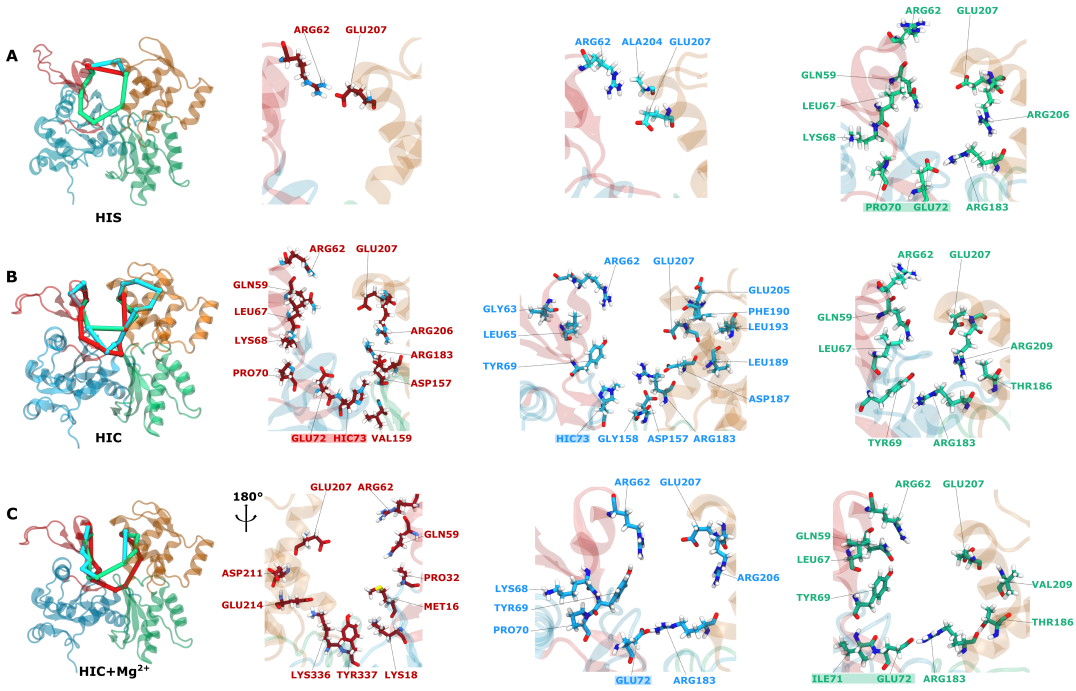

Figure 3. Correlations pathways in ATP-bound β-actin systems. Representation of 3 most represented pathways of communication between ARG62 and GLU207 for **A-** HIS73, **B-**HIC73 and **C-** HIC73+MG systems. Concerned amino acids are represented in licorice

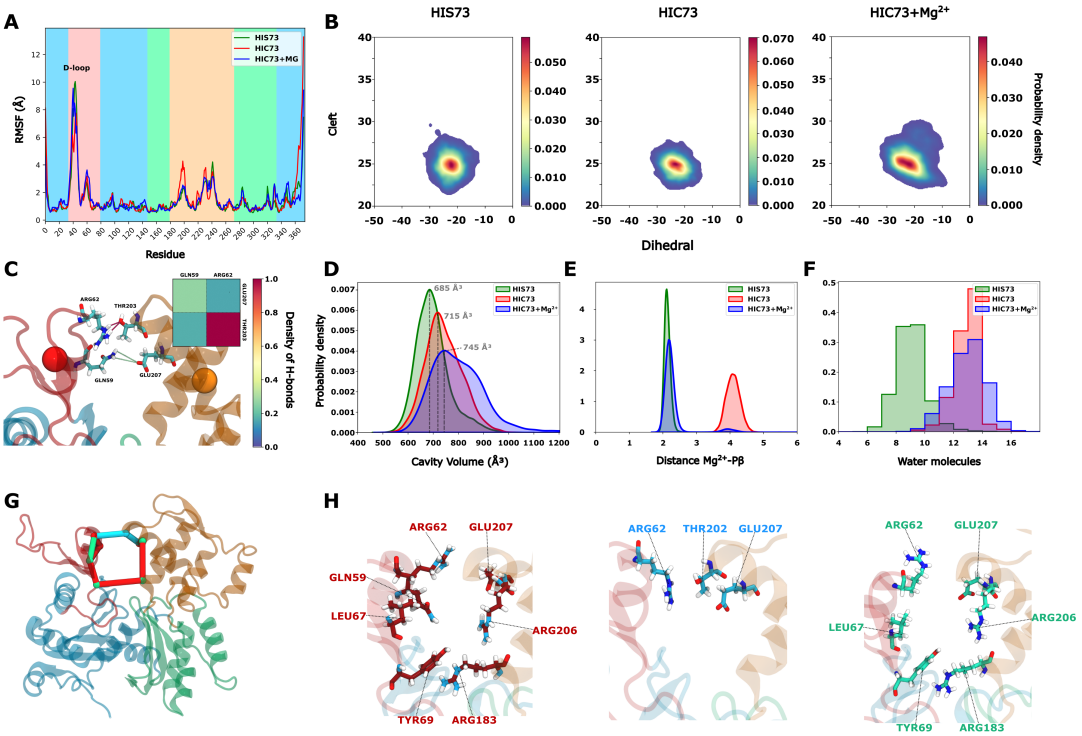

Figure 4. Replacement of ATP for ADP cancels the β-actin dynamics. A- RMSF of ADP-Actin systems. **B-** Cleft-Dihedral maps of ADP-Actin systems. **C-** Main H-bonds between SD2-SD4 subdomains in ATP-HIC system. **D-** Cavity volume of ADP-Actin systems. **E-** Distance between β phosphate of ADP and magnesium ion inside the cavity. **F-** Number of water molecules located at less than 5Å from the magnesium ion of the cavity. **G-** Representation of three most represented shortest paths between ARG62 and GLU207 in ADP-HIC system and **H-** Licorice representation of involved amino acids. Pathways of HIS and HIC+Mg systems are available in Fig S4

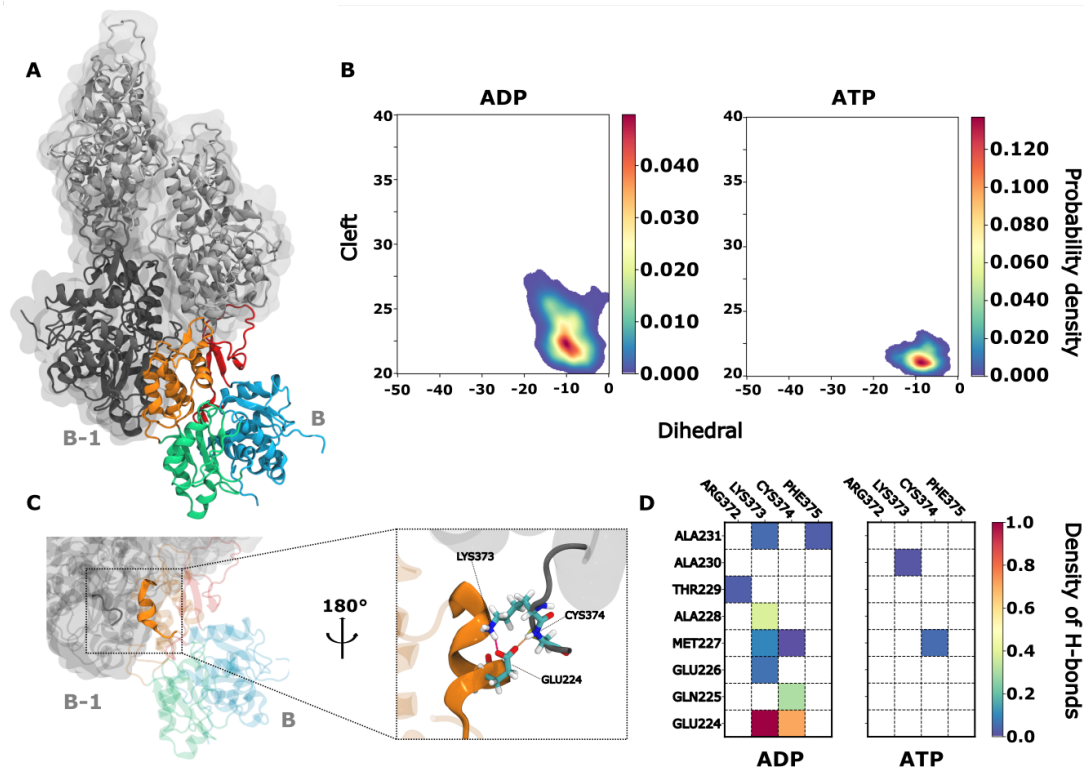

Figure 5. Nucleotide dependant fluctuations of the barbed end. Upper panel: Representation of subunit B (colored) and B-1 (Dark Grey). Distribution of Cleft-Dihedrals angles for B subunits in ADP and ATP states. **Lower Panel:** Highlight of C-terminal extremity of B-1 subunit and 220-230 helix of subunit B. Representation of the highest hydrogen bonds between C-terminal extremity of B-1 subunit and 220-230 helix of subunit B. Density of hydrogen bonds between C-terminal extremity of B-1 subunit and 220-230 helix of subunit B in ADP and ATP state